Experimental field analysis of damage-failure transition in composite material with a stress concentrator under cyclic loading (application of DIC and X-ray tomography techniques)

Mikhail Bannikov
Institute of Continuous Media Mechanics of the Ural Branch of the Russian Academy of Sciences, Perm, Russia
mbannikov@icmm.ru, http://orcid.org/0000-0002-5737-1422

Yuriy Bayandin, Aleksandr Nikityuk, Sergey Uvarov, Oleg Naimark
Institute of Continuous Media Mechanics of the Ural Branch of the Russian Academy of Sciences, Perm, Russia
buv@icmm.ru, http://orcid.org/0000-0002-1824-1940
nas@icmm.ru, https://orcid.org/0000-0001-6777-7525
usv@icmm.ru, https://orcid.org/0000-0002-7538-0971
naimark@icmm.ru, http://orcid.org/0000-0001-6537-1177

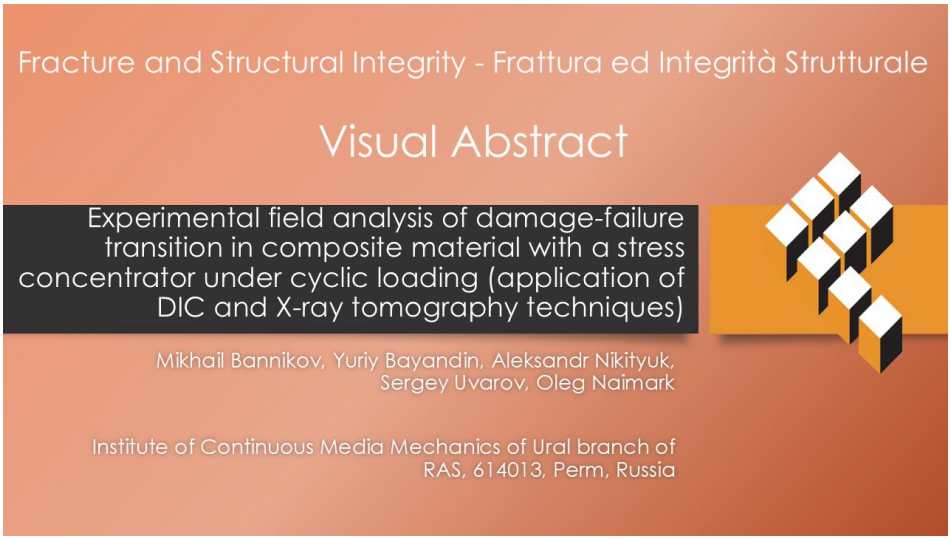

Citation: Bannikov, M., Bayadin, Y., Nikityuk, A., Uvarov, S., Naimark, O., Experimental field analysis of damage-failure transition in composite material with a stress concentrator under cyclic loading (application of DIC and X-ray tomography techniques), Fracture and Structural Integrity, 75 (2026) 238-249.

Received: 30.08.2025
Accepted: 24.10.2025
Published: 02.11.2025
Issue: 01.2026

KEYWORDS. Composites, Carbon fiber material, Defects, Damage, Microtomography, DIC.

INTRODUCTION

The confluence of mechanical characteristics and enhanced manufacturing technology of polymer composite materials has engendered a persistent trend towards their utilization in mechanical engineering, particularly within the domain of aviation [1,2] where cyclic fatigue with variable amplitude predominates as the primary loading factor.

The assessment of the stages of destruction of such materials is imperative in order to evaluate their long-term durability during operation. Recent experimental studies in the field of static and cyclic crack resistance, numerical modelling, have indicated a significant influence of various factors on the stress-strain state and crack resistance characteristics in the vicinity of the crack tip. These factors include the size of cracks and concentrators, the geometry of samples, and the type of loading. The study offers a promising avenue for substantiating models that facilitate the generalization of results on the failure staging in standard samples with a crack into the crack resistance of a structural element with stress concentrators. This is achieved by introducing an additional criterion parameter that reflects the stress-strain state in the vicinity of the concentrators, namely the tip of the crack.

The transition from damage to failure can be subdivided into characteristic stages according to the localization degree, which can be interpreted on the basis of self-similar solutions reflecting the characteristic spatial-temporal damage kinetics. Damage occurs at the initial stages of material deformation, and failure is associated with the development of cracks. In the initial phases of destruction, microcracks emerge, leading to their localization and subsequent formation. The processes of material damage are concentrated at the crack front, in the so-called "process zone", which ensures crack propagation. A comprehensive understanding of the physics and mechanics of the transition from damage to destruction is essential for the creation of models and the formulation of criteria for the mechanics of destruction. Such understanding enables the reflection of the relationship between the micromechanisms of damage development and the stages of destruction.

The employment of contemporary research methodologies, such as Digital Image Correlation (DIC), facilitates the real-time capture of loading processes and the subsequent construction of strain and stress fields within samples. DIC analysis is a valuable tool for estimating the values of residual stresses in composites [3], investigating the mechanisms of degradation of interlayer joint stiffness [4-6], and predicting fatigue crack growth under conditions of cyclic loads with variable amplitude, simulating a flight cycle [7].

The outcomes of a study by Lomov et al. [8] present a detailed examination of micro-CT observations, encompassing quantitative analysis and interpretation. This study was conducted in two phases: firstly, during the test and secondly, post-mortem. It focuses on the early stages of specimen loading, during which composites experience cracking at the micro- and meso-scales. This leads to the occurrence of multiple interacting damage modes across various scales. These include matrix cracking, fibre-matrix debonding, shear band formation, cracking in matrix pockets, and delamination, both local and large-scale. Complementing this approach, the work of Yuansong Wang et al. [9] demonstrates the powerful synergy of *in-situ* X-ray computed tomography with deep machine learning and digital volume correlation (DVC). Their research on notched woven CFRP composites under uniaxial tension successfully characterized the evolution of internal damage, identifying key modes such as fiber breakage and longitudinal/transverse cracks. Crucially, they showed that the integration of DVC and AI-based segmentation allows for accurate prediction of damage locations and initiation before ultimate failure, providing a dynamic 3D perspective on the damage kinetics in the process zone.

The efficacy of this multi-technique approach is further evidenced in studies of complex loading scenarios. For instance, Liang et al. [10] combined X-ray tomography, acoustic emission, and DIC to elucidate the flexural progressive failure mechanism of hybrid 3D woven composites. Their work revealed how hybrid structures (Carbon/UHMWPE) significantly influence mechanical behavior and damage modes, with distinct failure mechanisms—such as matrix cracking and debonding in warp-oriented specimens versus delamination in weft-oriented specimens—being clearly identified through the correlation of data from all three methods. Similarly, Djabali et al. [11] provided a thorough investigation of fatigue damage evolution in thick composite laminates under bending load by integrating X-ray tomography, AE, and DIC. Their combination allowed for the precise identification and quantification of damage, linked AE signals to specific physical damage origins, and monitored strain field evolution, thereby offering a complete description of the damage process during fatigue. The formation of fibre break clusters under synchrotron radiation computed tomography (CT) was presented in [12,13].

The present study examined the identification of successive damage staging, corresponding thresholding and concurrent use of acoustic emission, in-situ DIC and microscopy, post-mortem microscopy and X-ray inspection in quasistatic tensile tests and fatigue loading [14-16]. The principal novelty of this research consists in the development of a methodology that couples DIC and micro-tomography to decipher the mechanisms of damage accumulation. The derived clusters, corresponding to specific damage modes (e.g., matrix cracking, delamination, fiber breakage), are then used to construct a predictive model for failure progression in composites with stress concentrators. This data-driven approach enables a transition from phenomenological observation to a quantifiable prediction of residual life and structural integrity

MATERIALS AND METHODS

Specimens of woven polymer composite material with a hole

Quasi-static tension testing of unidirectional carbon fiber-reinforced polymer (CFRP) samples, with simultaneous acoustic emission signal recording and digital image correlation (DIC) analysis, was previously conducted by a team of authors and described in the works of [17-18]. In the current study, we investigate the stage-wise cyclic failure of composite materials, for which specimens with a stress concentrator in the form of a hole were selected. The stress concentrator ensured strain localization for convenient DIC analysis during the actual cyclic testing and subsequent examination of a sample taken from the most damaged area using X-ray tomography [19-21].

The composite material specimens were fabricated from CW200-TW2/2 2×2 twill weave fabric with an epoxy matrix, using an even number of layer pairs oriented at 0/45/90/-45° relative to the loading axis. The specimens were manufactured as 3-mm-thick strips measuring 25 × 250 mm, with bonded tabs made of the same material at the edges. A 6-mm hole was machined, using a diamond core drill, at the centre of each specimen to introduce a stress concentrator. The specimen geometry is shown in Fig. 1.

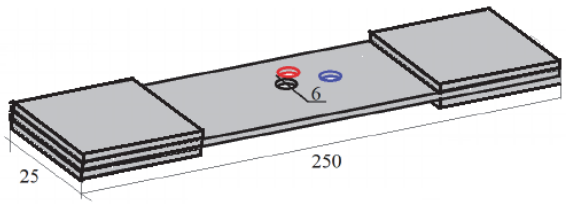

Figure 1: Specimen's geometry. The places for sampling for the analysis of the damage structure by X-ray tomography are shown in different colors: blue - away from the stress concentrator, red - nearby.

Experimental setup for cyclic testing

Cyclic loading was performed using a BISS 100 kN servo hydraulic universal testing machine at a frequency of 1 Hz with a load ratio of R=0.1, employing a block loading method with progressive amplitude increase from 50% to approximately 75% of the ultimate failure load, Fig.2. The specimen was mounted in the testing machine grips with its longitudinal axis aligned with the loading direction, ensuring the gripping conditions neither induced failure in the clamping area nor allowed slippage during testing. The Strain Master measurement system was utilized for in situ recording of displacement fields through digital image correlation (DIC), with subsequent conversion into strain fields, strain rate fields, and strain gradient fields at various time intervals with a 0.1 s time step. To assess the influence of damage accumulation on the failure progression stages, temporal and spatial phase portraits of the strain tensor component in the tensile direction were analyzed in phase coordinates.

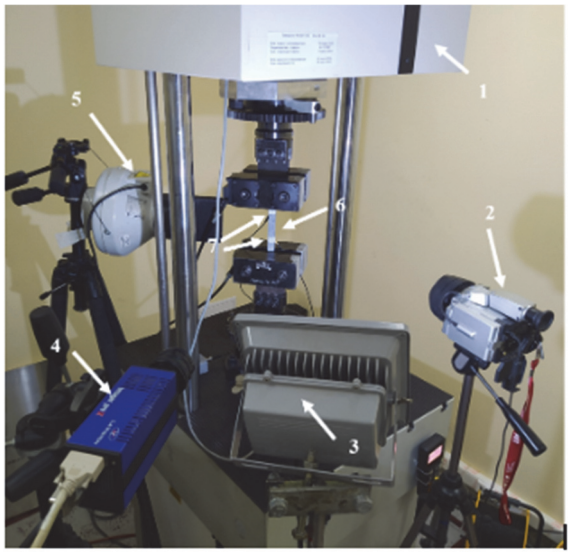

Figure 2: Experimental set-up cyclic testing. 1- Testing machine; 2 – IR camera; 3 - Illuminator, 4 – DIC camera, 5 - Cooling system, 6 – Specimen, 7 - Acoustic emission sensors.

Methods of analysis of fluctuations of the deformation field

The strain field fluctuations $\varepsilon_{yy}(t)$ of the specimen, derived through spatial averaging over the localized crack initiation zone, are analyzed while excluding the first harmonic component. Signal harmonics are identified through analysis of the amplitude-frequency spectrum generated by Fourier transformation:

$$\hat{\varepsilon}_{yy}(f)=\frac{1}{\sqrt{2\pi}}\int_{-\infty}^{\infty}e^{-itf}\varepsilon_{yy}(t)dt \tag{1}$$

$$A(f)=\left|\hat{\varepsilon}_{yy}(f)\right| \tag{2}$$

where f and A – the frequency and amplitude of fluctuations of the deformation field, respectively, ^ – a Fourier transform. To eliminate the oscillations corresponding to the first harmonic, filtering based on forward and reverse wavelet transforms is used

$$W(k,b)=\int_{-\infty}^{\infty}|k|^{-1/2}\psi\left(\frac{t-b}{k}\right)^{*}\varepsilon_{yy}(t)dt \tag{3}$$

$$\varepsilon_{yy}(t)=C_{\psi}^{-1}\int_{-\infty}^{\infty}\int_{-\infty}^{\infty}W(k,b)\psi_{k,b}(t)\frac{dk\,db}{k^{2}} \tag{4}$$

$$C_{\psi}=2\pi\int_{-\infty}^{\infty}\frac{\left|\hat{\psi}(\xi)\right|^{2}}{|\xi|}d\xi \tag{5}$$

where W are the wavelet coefficients obtained by applying the direct wavelet transform, k is the scale parameter, b is the spatial parameter, ψ is the analysing wavelet, as which the Morlet wavelet is used in this work, C_{ψ} is the normalizing coefficient.

The rate fluctuations changing in the deformation field of the sample is calculated according to the following ratio

$$\frac{\partial\varepsilon_{yy}(t)}{\partial t}=\frac{\varepsilon_{yy}(t-1)-2\varepsilon_{yy}(t)+\varepsilon_{yy}(t+1)}{2dt}. \tag{6}$$

For every loading block in the cyclic tests of the notched composite specimen, phase trajectories are visualized in the space $\varepsilon_{yy}(t)$, $\partial\varepsilon_{yy}(t)/\partial t$ in order to characterize the progressive damage accumulation behaviour.

X-ray tomography analysis near and far from the stress concentrator area

Cylindrical specimens (Ø2 mm × 3 mm) were extracted from regions of peak (Fig. 1, point 2) and baseline strain using diamond core drilling. X-ray tomography studies were conducted after interrupted loading at 85% ultimate tensile strength to capture stress concentrator evolution.

Cylindrical tomography samples were extracted from both stress-concentrator and low-strain regions (Fig. 1) and analyzed using synchrotron X-ray radiation (SR) from the VEPP-3 electron accelerator's wiggler station (the Budker Institute of Nuclear Physics, SB RAS). The SR beam exhibited 0.1 mrad angular divergence, 0.1 kW total power, and 1 μm spatial resolution in the 5–30 keV energy range, with the full experimental setup detailed in Fig. 3.

Tomographic imaging was performed using 4-μm-thin scintillation screens. A high-resolution Hamamatsu ORCA-Flash 2.8 CCD detector (2048×2048-pixel array) was employed, providing an effective pixel size of 0.6 μm after accounting for objective magnification. The experimental setup maintained precise alignment of the sample, scintillator, and detector with positioning accuracies of ±1 μm in linear coordinates and ±0.001° in angular coordinates relative to the X-ray beam. Beam collimation was achieved using a 1.5×1.5 mm square aperture

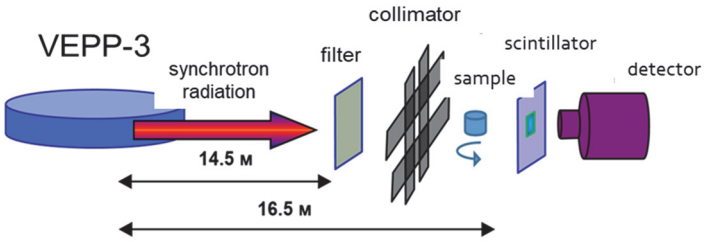

Figure 3: The principal scheme for conducting research using the microtomography method.

The tomographic data were processed in ImageJ/Fiji using global threshold segmentation to reconstruct 3D density matrices (800×800×601 voxels at 2.6 μm resolution), capturing the material's internal structure. Derivative matrices were generated to analyze spatial heterogeneity and visualize porosity distribution.

Pore characteristics—volume, surface area, and centroid coordinates—were extracted using the 3D Objects Counter, enabling calculation of inter-pore distances and morphological metrics such as the surface-area-to-volume ratio (dispersion factor). Structural orientation was assessed layer-wise using OrientationJ, yielding coherence values from 0 (random) to 1 (aligned) to quantify organizational uniformity.

Porosity data were clustered using a Bayesian Gaussian Mixture algorithm in Python, which autonomously identifies the optimal number of statistical distributions—unlike standard methods—providing a more adaptive and robust analysis of pore regimes, as supported by previous studies [19-21].

RESULTS

Results of cyclic testing for woven CFRP specimens with a hole

The cyclic loading experiment, with strain field monitoring via digital image correlation (DIC), employed a block-loading protocol with stepwise amplitude increases—from a nominally safe level (surviving >500k cycles under constant load) to a critical amplitude (causing failure within <1k cycles). Acoustic emission data were recorded concurrently throughout the tests. The duration of each loading block (1k–1.5k cycles) was selected based on analysis to ensure a sufficient number of AE hits for reliable statistical and subsequent cluster analysis, allowing the signals to stabilize in terms of cumulative energy and event rate at each load level. The initial block was set longer (>50k cycles) to establish a baseline for damage initiation under low load. The corresponding load amplitudes and cycle counts for each block are detailed in Tab. 1.

№ block	Loading amplitude, MPa	Number of cycles
1	345	56000
2	350	1950
3	355	1150
4	360	2000
5	365	1410
6	370	1190
7	375	1300
8	380	1200
9	385	1200
10	390	1100
11	395	1300
12	400	1200
13	405	1100
14	410	600, Failure

Table 1: – Block loading of a composite specimen with a hole.

Fig. 4 presents strain distributions at specific time points corresponding to loading blocks 12 (Fig. 4, a) and 14 (Fig. 4,b). A 7×7-pixel black square marks the crack initiation zone, where strain values were averaged to generate one-dimensional

signals for subsequent analysis. The figure clearly reveals strain localization areas that coincide with crack formation sites. The DIC analysis was performed using a spatial resolution of 5 pixels/mm. The progression of high Δεyy values provides a sensitive indicator of ongoing damage processes before they become macroscopically visible. This quantitative map of strain fluctuations is then directly compared with the internal damage observed via X-ray tomography in the subsequent figures, validating its use as a precursor signal for damage. The strain fields were calculated from the full-field displacement data provided by the DIC system. The Green-Lagrange strain tensor was computed over a subset of neighbouring pixels using a (3×3) pixel strain filter window.

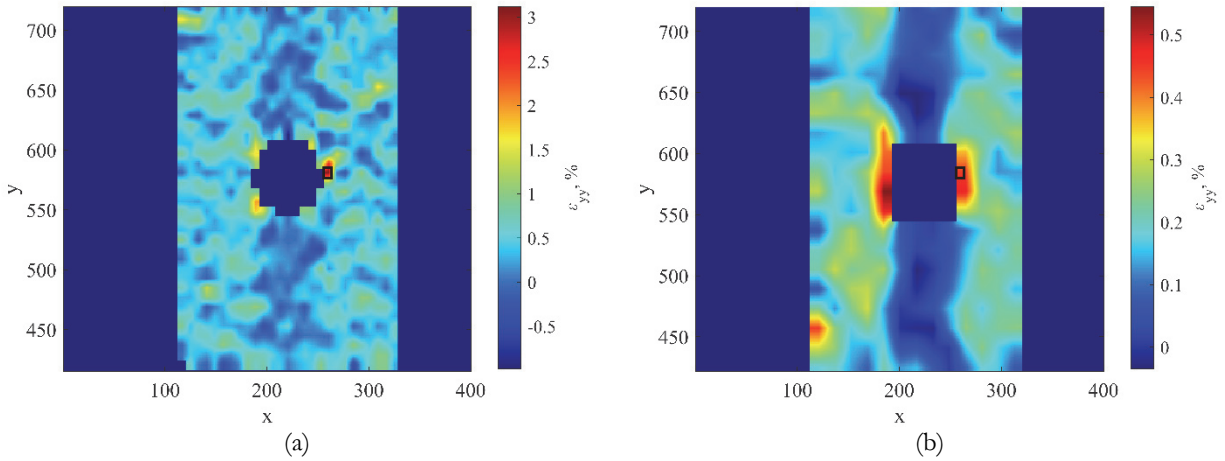

Figure 4: The deformation fields at time corresponding to 12 (a) and 14 (b) loading blocks. The averaging area is highlighted by a black square.

Analysis of fluctuations of deformation fields

Fig. 5 presents typical results of the signal extraction procedure used for subsequent phase portrait calculation. The original signal (Fig. 5, a) represents strain field fluctuations in the crack development zone (see Fig. 4). Fourier transformation and amplitude-frequency spectrum analysis (Fig. 5, b) reveal multiple harmonic components in the signal, with the dominant first harmonic at 1 Hz. The full-field strain (ε_{yy}) was directly obtained from the DIC system. However, to isolate the local strain concentrations from the global, far-field strain gradient caused by the stress concentration around the hole, the first-order (linear) trend was subtracted from the data. This process, often referred to as 'detrending,' amplifies the visibility of local anomalies that are critical for identifying early damage initiation sites. To eliminate its influence, we: (1) extracted the first harmonic component (white dashed lines in Fig. 5, c marks the region of interest) using continuous wavelet transform (both forward and inverse), and (2) subtracted it from the original strain field fluctuations (Fig. 5, d). As seen in Fig. 5d, the strain signal, while resulting from a constant amplitude load, exhibits significant cycle-to-cycle variability. This is interpreted as a direct consequence of damage accumulation, which continuously alters the local stiffness of the material specimen.

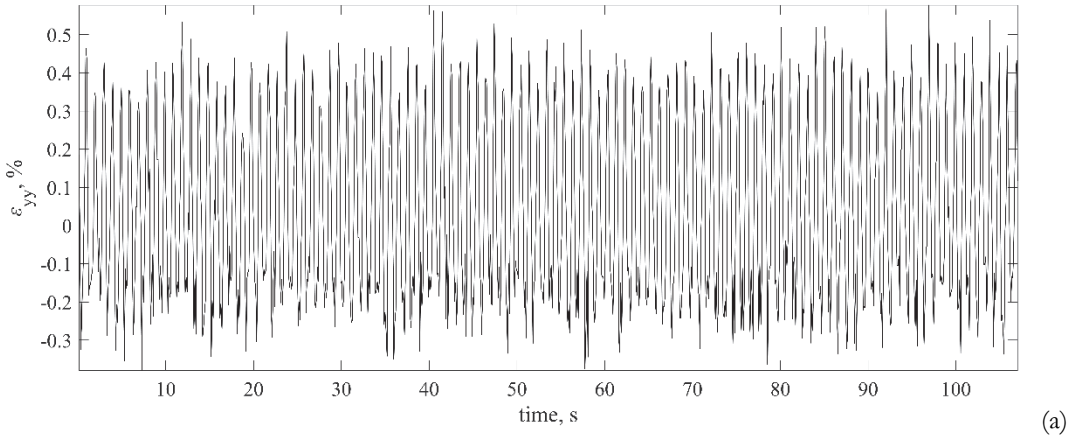

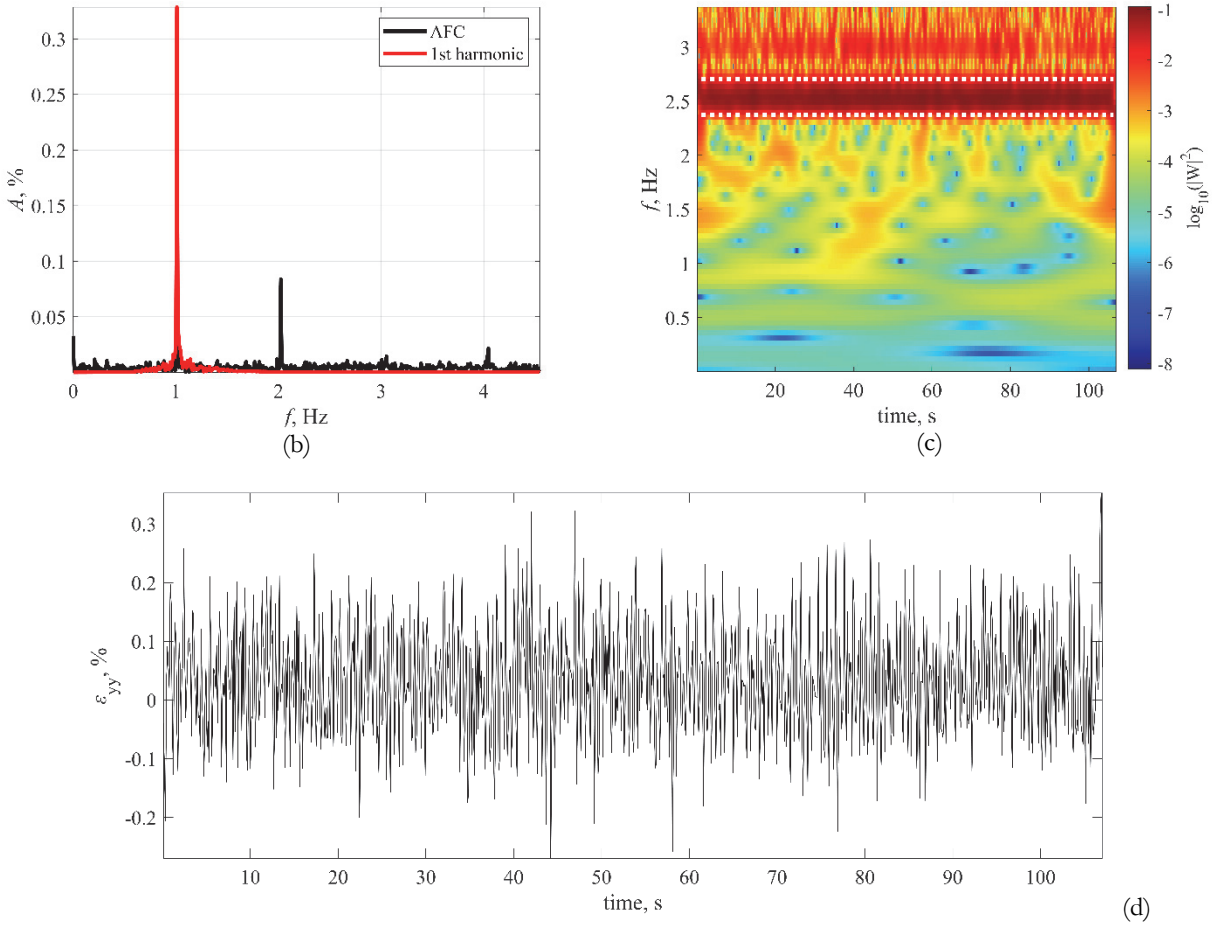

Figure 5: Signal processing workflow: (a) Strain-time dependence (raw signal); (b) Amplitude-frequency characteristics of: the original signal (black) and first harmonic component (red) obtained through wavelet filtering; (c) Squared modulus of wavelet coefficients (time-frequency representation). White dashed lines indicate the first harmonic frequency band; (d) Filtered strain-time dependence after first harmonic subtraction.

Fig. 6 presents phase portraits of strain field fluctuations in the crack propagation zone, subdivided into two parts to visually separate the evolving trends: (a) loading blocks 1-7 and (b) blocks 8-14. This subdivision clearly reveals two distinct macroscopic regimes. The initial stage (blocks 1-7) is characterized by progressive shifting and expansion of the phase portraits, indicating a gradual increase in both strain and strain rate during distributed damage accumulation.

A fundamental transition occurs in the final blocks (8-14). The phase portrait of the final 14th block itself can be deconvoluted into two distinct components, each associated with a different dynamic attractor. The first, a highly concentrated and stable attractor, signifies the regime of localized propagation of the main crack. The second, manifested as a "random" point cloud, corresponds to a self-similar solution describing the singular temporal kinetics of fracture nucleation (daughter crack formation). This coexistence reveals the collective and multi-scale nature of the damage evolution, where the distributions in "strain - strain gradient" coordinates capture the interplay between the stress field singularity at the macro-crack tip and stochastic micro-damage events in the process zone. The emergence of the dominant macro-crack attractor marks the conclusive transition from distributed damage to an unstable phase of critical crack growth, culminating in final fracture.

X-ray tomography data analysis

Microtomographic examination was primarily focused on the area adjacent to the stress concentrator (Fig. 7a). This region was of particular interest as it revealed the existence of transverse cracks (Fig. 7c) in specific composite layers, in addition to a population of pores (Fig. 7b). The results of the cluster analysis revealed a strong positive covariance between the volume and surface area of pores across all studied samples of the carbon composite material [18]. Although the pores were consistently separated into two clusters ("small" and "large" based on conventional criteria), the key differentiating parameter

was the variation in surface area rather than volume. This suggests that while the overall bifurcation model is consistent, the pore formation process in each sample type results in unique geometric characteristics.

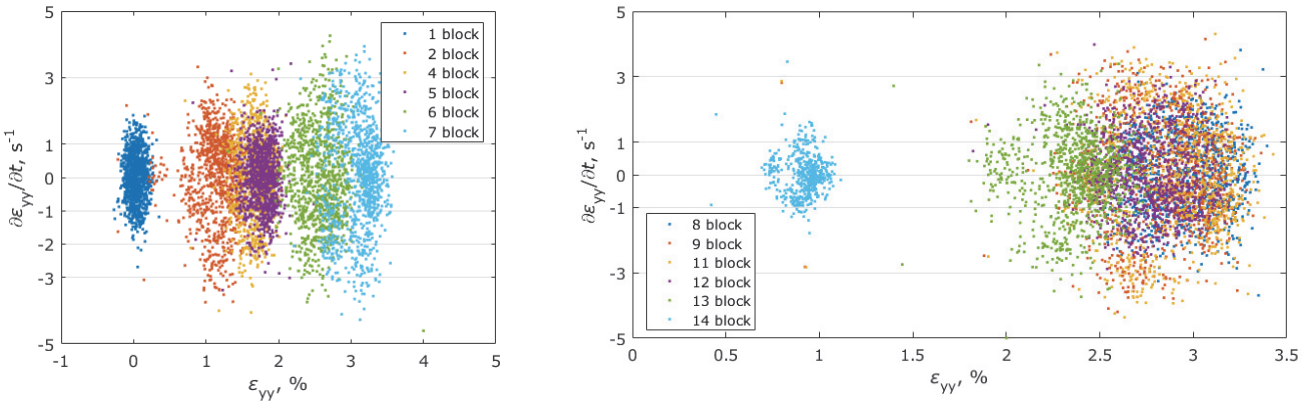

(a) (b)

Figure 6: Phase portraits of strain field fluctuations: (a) loading blocks 1-7; (b) loading blocks 8-14. In the phase portraits for blocks 13 and 14, a separation of the general point cloud into two distinct parts is observed, which is associated with the emergence of a new dynamic attractor.

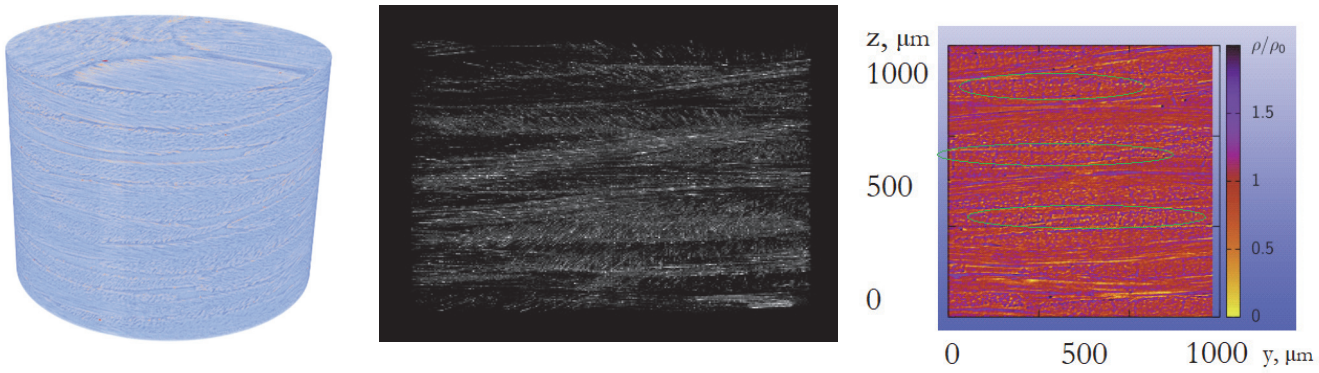

a) b) c)

Figure 7: a) Micro-CT image of sample near the stress concentrator, (b) Pore distribution in ZY section, c) ZY section of microtomography of a sample from the stress concentration area, transverse cracks are highlighted with green ovals.

It was found that undeformed samples were dominated (about 80%) by small pores with an average volume of 94 µm³ and a surface area of 192 µm². Under quasi-static loading within the stress concentrator zone, the average volume of small pores increased to 1238 µm³ and their surface area to 970 µm², while their proportion remained high (81%). The highest proportion of small pores (more than 90%) with parameters of 1124 µm³ and 1444 µm² was recorded in samples outside the concentrator zone. Under cyclic loading, the proportion of small pores was 84% (volume 997 µm³, surface area 1284 µm²), with a relative increase in the population of large pores compared to quasi-static loading [19].

The obtained data suggest the following model of deformation behavior for pores: an increase in mechanical load first leads to the growth of existing pores, and then to the nucleation of new damage. It is likely that under cyclic loading, the increase in pore size occurs unevenly. Pores located in close proximity to each other grow most intensively, leading to a reduction in the distance between them and their subsequent coalescence into large cavities.

The cluster analysis (fig. 8) revealed a low negative covariance between the pore dispersion factor (Square/Volume) and inter-pore distance, indicating these are largely independent characteristics. While pore clustering was primarily defined by distance, the dispersion factor mean decreased from 2.87 µm^{-1} in unloaded samples to ~1.83 µm^{-1} under mechanical loads, and the proportion of far-spaced pores increased significantly, reaching 52.88% near the stress concentrator. The previous observation [19-21] allows us to conclude that pores that are located in close proximity to each other under mechanical loading are most likely to increase in size and merge, forming new, larger defects such as delamination and cracking. Therefore, the proportion of closely spaced pores is a factor determining the strength of CFRP samples.

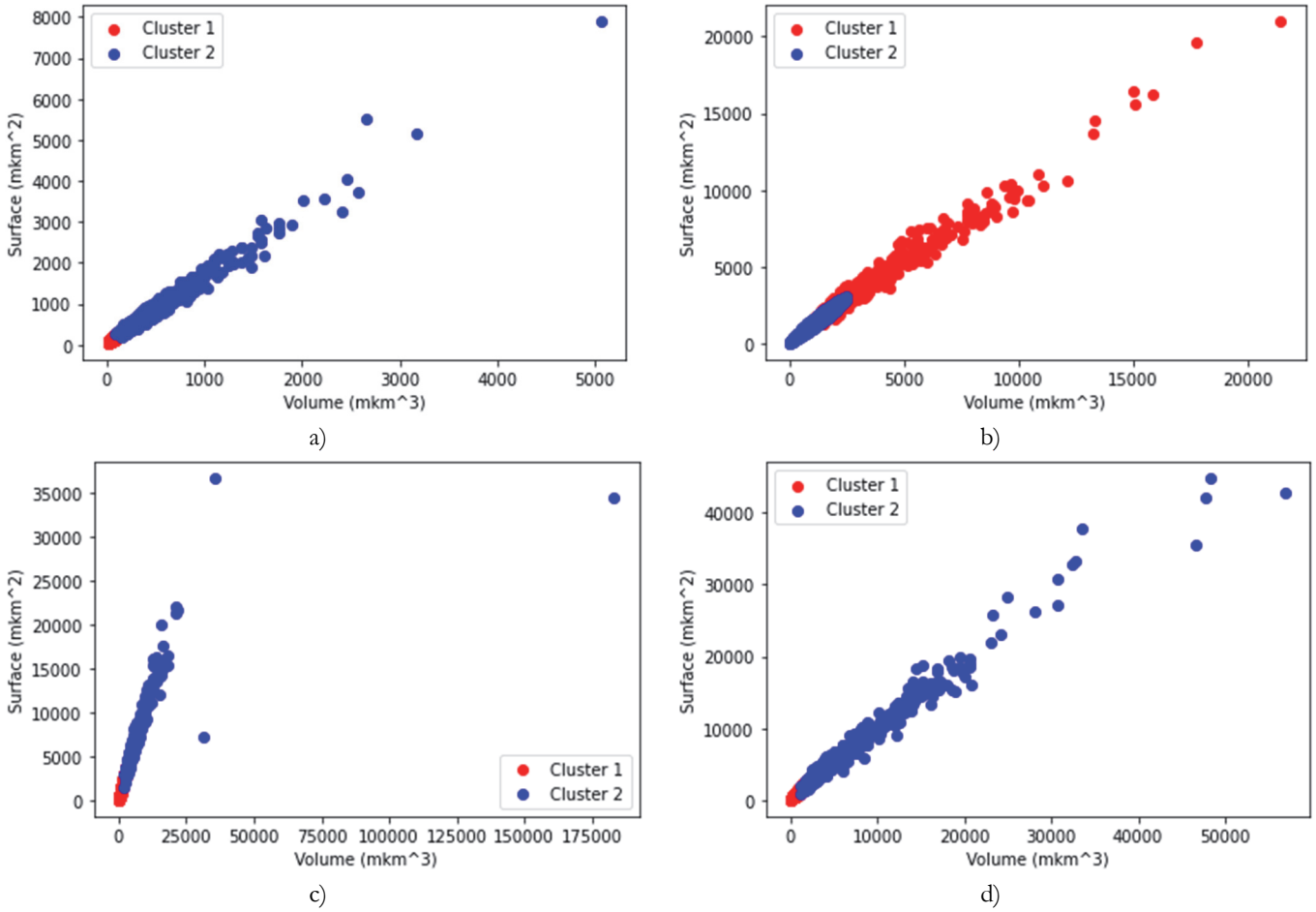

Figure 8: The following diagrams illustrate the results of cluster analysis by volume and surface area for the following samples: (a) without loading (initial state); (b) after quasi-static loading in the stress concentrator area; (c) after quasi-static loading far from the stress concentrator area; (d) after cyclic loading far from the stress concentrator area [19].

In particle sedimentation analysis, the geometric features of roundness and sphericity are of utility. The definition and application of these parameters for rock fragment analysis and a review of geometric characterization in relation to X-ray imaging data is presented in work [19]. In addition to the previously defined geometric parameters, a new parameter, sphericity, is introduced for the analysis of pore distribution:

$$Sphericity = \frac{\left(36\pi V^2\right)^{1/3}}{S} \tag{7}$$

where V – volume of pore, S – its square. Fig. 9 illustrates the pore distribution in logarithmic coordinates with respect to sphericity and size. It can be observed that the distribution of defects as a function of sphericity versus size is consistent with a power law. The log-log plot additionally demonstrates a slope line with a value of -1. For samples exhibiting technological (major) defects, values that deviate from this dependence are observed. The analysis of pore volume/area variable distribution data using geometric supplementary parameters (roundness, sphericity, anisogeometricity, anisotropy) may facilitate a more detailed classification of defects.

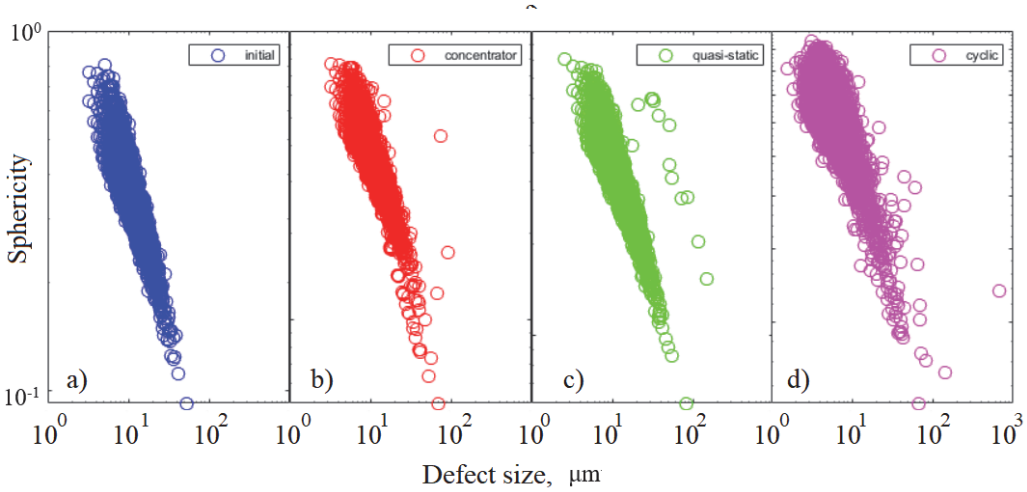

Figure 9: Sphericity versus equivalent size of pores: (a) without loading (initial state); (b) after quasi-static loading in the stress concentrator area; (c) after quasi-static loading far from the stress concentrator area; (d) after cyclic loading far from the stress concentrator area.

CONCLUSION

This study established a methodology for correlating the integral structural characteristics of carbon fiber composites with their damage evolution under mechanical load. By combining in-situ microtomography with digital image correlation (DIC), we directly observed the transition from distributed damage accumulation to macroscopic failure. Analysis of the strain fields revealed that the temporal strain distributions at the point of most intense deformation form compact point clusters, reflecting the hyperbolic nature of the stress field near the crack tip, consistent with Irwin's self-similar solution. Furthermore, the distributions in "strain - strain gradient" coordinates unveiled collective effects in damage evolution while accounting for stress state singularities.

The core of our analysis employed two order parameters—pore volume and surface area—to quantify pore anisogeometry. A novel damage staging methodology was developed, combining microtomography-based threshold segmentation and cluster analysis of characteristic volumes in preloaded specimens. This approach revealed fundamentally different damage mechanisms under varying loading conditions:

Under quasi-static loading, a decrease in pore clustering and ordering was observed while the overall orientation distribution was maintained. Under cyclic loading, two distinct pore clusters emerged: one orientation-distributed and another with a pronounced transverse alignment.

A critical finding is that mechanical loading-induced pore proximity significantly increases the probability of pore expansion and coalescence, leading to the formation of larger critical defects such as delaminations and cracks. Consequently, the fraction of closely-spaced pores is a key determinant of ultimate strength in the studied materials. The sphericity parameter was found to follow a power-law distribution with pore size, though large, technology-related or deformation-induced defects exhibited significant deviations from this trend.

In summary, the developed multi-modal methodology provides a powerful framework for quantifying damage evolution and identifying critical microstructural parameters that control failure in composite materials, paving the way for more accurate life-prediction models.

AUTHOR CONTRIBUTION

Author contributions are following. Conceptualization: O.B.N. (Oleg B. Naimark); methodology M.V.B. (Mikhail V. Bannikov), Aleksandr S. Nikitiuk, Sergey V. Uvarov, Yuriy V. Bayandin; writing-original draft preparation: O.B.N., M.V.B.

ACKNOWLEDGEMENTS

The work was carried out as part of a major scientific project funded by the Ministry of Science and Higher Education of the Russian Federation (Agreement No. 075-15-2024-535 dated 23 April 2024).

REFERENCES

[1] Zolkin, A.L., Galanskiy, S. A. and Kuzmin, A. M. (2021). Perspectives for use of composite and polymer materials in aircraft construction IOP Conference Series: Materials Science and Engineering. 1047, 012023. DOI: https://doi.org/10.1088/1757-899X/1047/1/012023

[2] Kesarwani, S. (2017) Polymer composites in aviation sector. International Journal of Engineering Research & Technology (IJERT). 6(6). DOI: http://dx.doi.org/10.17577/IJERTV6IS060291

[3] Rastak, M.A., Shokrieh, M.M., Barrallier, L., Kubler, R. and Salehi, S.D. (2021) Estimation of residual stresses in polymer-matrix composites using digital image correlation. In: Shokrieh, M.M. (ed.) Residual Stresses in Composite Materials. 2nd edn. Woodhead Publishing, pp. 455–486.

[4] He, Z., Luo, Q., Li, Q., Zheng, G. and Sun, G. (2022) Fatigue behavior of CFRP/Al adhesive joints — Failure mechanisms study using digital image correlation (DIC) technique. Thin-Walled Structures. 174, 109075. DOI: https://doi.org/10.1016/j.tws.2022.109075

[5] Orell, O., Jokinen, J. and Kanerva, M. (2023) Use of DIC in the characterisation of mode II crack propagation in adhesive fatigue testing. International Journal of Adhesion and Adhesives. 122, 103332. DOI: https://doi.org/10.1016/j.ijadhadh.2023.103332

[6] Chen, Y., Yang, J., Qiu, X., Ji, C. and Wang, B. (2023) DIC-based constant amplitude and two-block loading fatigue life prediction of open hole GLARE laminate. Engineering Fracture Mechanics. 278, 109016. DOI: https://doi.org/10.1016/j.engfracmech.2022.109016

[7] Khan, S.U., Alderliesten, R.C., Rans, C.D. and Benedictus, R. (2010) Application of a modified Wheeler model to predict fatigue crack growth in Fibre Metal Laminates under variable amplitude loading. Engineering Fracture Mechanics. 77(9), 1400–1416. DOI: https://doi.org/10.1016/j.engfracmech.2010.03.041

[8] Lomov, S.V., Breite, C., Carrella-Payan, D., Carvelli, V., Ersoy, N., Gigliotti, M. and Gorbatikh, L. (2018) Multi-instrument multi-scale experimental damage mechanics for fibre reinforced composites. IOP Conference Series: Materials Science and Engineering. 406, 012057. DOI: https://doi.org/10.1088/1757-899X/406/1/012057

[9] Wang Y., Chen Q., Luo Q., Li Q., Sun G., (2024) Characterizing damage evolution in fiber reinforced composites using in-situ X-ray computed tomography, deep machine learning and digital volume correlation (DVC), Composites Science and Technology, 254, 110650. DOI: https://doi.org/10.1016/j.compscitech.2024.110650.

[10] Liang Q., Liu J., Wang X., Liu X., Zhang D., Qian K., (2022) Flexural progressive failure mechanism of hybrid 3D woven composites: Combination of X-ray tomography, acoustic emission and digital image correlation, Composite Structures, 280, 114894. DOI: https://doi.org/10.1016/j.compstruct.2021.114894.

[11] Djabali A., Toubal L., Zitoune R., Rechak S., (2019) Fatigue damage evolution in thick composite laminates: Combination of X-ray tomography, acoustic emission and digital image correlation, Composites Science and Technology, 183, 107815. DOI: https://doi.org/10.1016/j.compscitech.2019.107815.

[12] Gu, Q., Quan, Z., Yu, J., Yan, J., Sun, B. and Xu, G. (2019) Structural modeling and mechanical characterizing of three-dimensional four-step braided composites: A review. Composite Structures. 207, pp. 119–128. DOI: https://doi.org/10.1016/j.compstruct.2018.09.065

[13] Magalhaes, A.G. and De Moura, M.F.S.F. (2005) Application of acoustic emission to study creep behaviour of composite bonded lap shear joints. NDT & E International. 38(1), pp. 45–52. DOI: https://doi.org/10.1016/j.ndteint.2004.06.005

[14] Carvelli, V., D'Ettorre, A. and Lomov, S.V. (2017) Acoustic emission and damage mode correlation in textile reinforced PPS composites. Composite Structures. 163, pp. 399–409. DOI: https://doi.org/10.1016/j.compstruct.2016.12.012

[15] Carvelli, V., Jain, A. and Lomov, S.V. (2017) Fatigue of textile and short fiber reinforced composites. John Wiley & Sons.

[16] Gorbatikh, L. and Lomov, S.V. (2016) Modeling Damage, Fatigue and Failure of Composite Materials. In: Talreja, R. & Varna, J. (eds.) Modeling Damage, Fatigue and Failure of Composite Materials. Woodhead Publishing, pp. 41–59.

[17] Ivanov, S.G., Beyens, D., Gorbatikh, L. & Lomov, S.V. (2017) Journal of Composite Materials. 51(5), pp. 637–647.

DOI: https://doi.org/10.1177/0021998316653460

[18] Bannikov, M., Sazhenkov, N., Balakirev, A., Sazenkov, N., Uvarov, S., Bayandin, Y., Nikitiuk, A., Nikhamkin, M. & Naimark, O. (2022) Acoustic emission phase analysis of damage-failure transition staging in composite materials. Procedia Structural Integrity. 41, pp. 518–526. DOI: https://doi.org/10.1016/j.prostr.2022.05.059

[19] Naimark, O.B., Uvarov, S.V., Bannikov, M.V., Bayandin, Yu.V. and Nikityuk, A.S. (2022). Critical Dynamics of Damage to Composites and Two-Parameter Fracture Criteria. Journal of Engineering Physics and Thermophysics. 95, pp. 1652–1658. DOI: https://doi.org/10.1007/s10891-022-02634-4

[20] Ignatova, A.M., Balakhnin, A.N., Bannikov, M.V., Kuper, K.E., Nikitiuk, A.S. and Naimark, O.B. (2022) Technique for obtaining an integral characteristic of the structure of a loaded composite material based on microtomographic research data. Procedia Structural Integrity. 41, pp. 550–556. DOI: https://doi.org/10.1016/j.prostr.2022.05.063

[21] Ignatova, A.M., Bannikov, M.V., Bayandin, Yu.V., Balakhnin, A.N., Kuper, K. E., Naimark, O.B., (2023). Macrostructural Characteristics Of Carbon Composite Based On Microtomographic Data, Procedia Structural Integrity, 47, pp. 820-825. DOI: https://doi.org/10.1016/j.prostr.2023.07.037.